

Noncurvature-driven modes in a transport barrier

B. N. Rogers

Department of Physics and Astronomy, Dartmouth College, Hanover, New Hampshire 03755

W. Dorland

Department of Physics, University of Maryland, College Park, Maryland 20742

(Received 21 October 2004; accepted 11 April 2005; published online 8 June 2005)

Transport barriers that form in both the edge and interior regions of high temperature magnetically confined discharges are characterized by steep plasma gradients, strong $\mathbf{E} \times \mathbf{B}$ and diamagnetic flows, and varying levels of magnetic shear. This study addresses the linear stability of such configurations in the context of a simple slab model using both analytic calculations as well as numerical simulations from the gyrokinetic GS2 code. Three linear modes of potential importance are found: the Kelvin–Helmholtz instability, the tertiary mode, and a nonlocal drift wave instability. Each mode is unstable only in the presence of nontrivial spatial variations in either the $\mathbf{E} \times \mathbf{B}$ flow and/or the plasma gradients. The strongest conclusion of this study is that the drift wave mode may be an important driver of anomalous transport in the edge region of magnetic confinement devices. Two other weaker conclusions that warrant further study are as follows: (1) the Kelvin–Helmholtz instability may be associated with edge-localized modes or edge transport and (2) the tertiary mode can potentially limit the radial growth of a transport barrier. © 2005 American Institute of Physics. [DOI: 10.1063/1.1928250]

I. INTRODUCTION

This paper explores the linear stability of simple slab plasma configurations without magnetic curvature using both analytic and numerical studies. Our numerical results are produced using the electromagnetic, gyrokinetic GS2 code,¹ while our analytic calculations are based on the Braginskii and gyrofluid models. The configurations we study are characterized by sheared $\mathbf{E} \times \mathbf{B}$ and diamagnetic flows, weak collisionality, and finite magnetic shear. Our main application of interest is the edge pedestal region of high temperature (e.g., H mode) tokamak discharges, but the results we obtain are also potentially relevant to internal transport barriers (ITBs), and to other physical systems. Our neglect of the magnetic curvature is motivated by the strong plasma gradients found in pedestals and ITBs, which we find are capable of driving instabilities with growth rates that surpass those of curvature-driven modes. Strong parallel flows, though sometimes present in laboratory fusion experiments, will be addressed in future work.

The simulations indicate the potential importance of at least three instabilities: the Kelvin–Helmholtz (KH) instability, the tertiary mode,² and a nonlocal drift wave instability. These instabilities are all global modes, in the sense that they are all dependent on nonlocal variations of the background “equilibrium” quantities, and are all absent from local simulations in which the background plasma gradients and the $\mathbf{E} \times \mathbf{B}$ shear V'_E (if present) are spatially constant. The latter two (the tertiary mode and the drift wave instability), on the other hand, are also quasilocal, in the sense that they can be radially localized to scales that are the geometric mean of the equilibrium scale and smaller scales, and are therefore sensitive to the profile variations only in a relatively small region. This makes some general analytic progress possible in

these cases through Taylor expansion of the background profiles.

Depending on the parameters, the KH instability is potentially the strongest instability of the three modes. Because of its magnetohydrodynamiclike (MHD-like) character and large radial scales (comparable to the barrier width), the onset of this instability might trigger a complete edge-localized-mode-like (ELM-like) collapse of the profiles. On the other hand, depending on the details of the nonlinear evolution (not calculated here), it might be associated mainly with transport. As is well known, in the simplest case of a shearless magnetic field with $k_{\parallel}=0$, the only requirement for instability is an inflection point in the background $\mathbf{E} \times \mathbf{B}$ flow V_E . This condition is usually satisfied in a H -mode edge pedestal, while in the case of ITBs, the prevalence of inflection points is less clear. In any case, given an inflection point, we address here two factors that can stabilize the KH mode: magnetic shear (moderately strong in the edge but weak in internal barriers) and ion diamagnetic effects (strong in both cases). In the presence of magnetic shear, it is impossible to satisfy $k_{\parallel}=0$ everywhere within the envelope of the mode, and so the mode can be stabilized by line bending if either the magnetic shear or the barrier width becomes sufficiently large. Estimates given later suggest that, due to the magnetic shear alone, the Kelvin–Helmholtz instability hovers near marginal stability in the H -mode edge. In the absence of magnetic shear, we show that ion diamagnetism alone can stabilize the mode if the ion diamagnetic velocity V_{*i} is at least comparable to V_E and in the opposite direction. Unless core velocity profiles in ITBs quite generally lack inflection points, the fact that KH instabilities are *not* observed to limit ITBs is likely due to these ion diamagnetic effects. With respect to H -mode pedestals, typical edge profiles from experimental observations, as well as the profiles predicted by

some numerical simulations, seem at least roughly close to the marginal case of $V_E + V_{*i} \approx 0$. A more detailed study that includes both realistic magnetic geometry and two-fluid effects is therefore needed to determine the precise role of the Kelvin–Helmholtz instability in the tokamak edge.

The tertiary mode, in contrast to the Kelvin–Helmholtz instability, arises at high k_{\parallel} and is characterized by an adiabatic electron response. It is driven by the ion temperature gradient, is radially localized by the $\mathbf{E} \times \mathbf{B}$ shear, and is insensitive to the magnetic shear. The equilibrium density gradient, studied here for the first time, also plays a complex role. According to the numerical calculations, this mode can be stabilized by finite Larmor radius (FLR) effects when the pedestal width becomes comparable to 5–10 ion Larmor radii. Thus, this instability is expected to be stable in narrow pedestals and unstable in wide pedestals. While the importance of this mode in the edge region will require further nonlinear study, we note that such a dependence (i.e., a mode that is unstable only in sufficiently wide pedestals) is potentially associated with the existence of a *maximum* pedestal width.

The nonlocal drift wave instability is a linear, edge-localized version of a nonlinear drift wave mode that has been widely studied in local turbulence simulations of the edge region.^{3–6} These turbulence simulations are typically carried out in the presence of spatially constant plasma gradient scale lengths and magnetic shear, and as is well known,⁷ radially localized, linearly unstable drift wave eigenmodes do not exist in such systems. Nonlinearly, however, drift wave physics is hypothesized to play an important role in driving small-scale turbulence at *H*-mode-like parameters in the edge region, where resistive ballooning modes are expected to become weak.^{3–6} We show here that in the presence of more realistic pedestal-like profiles in either the $\mathbf{E} \times \mathbf{B}$ velocity and/or the density gradient, a robustly unstable, radially localized linear eigenmode reappears in the simulations, with or without magnetic shear. This result is consistent with past theoretical studies of drift waves going back for decades, which have shown that strong spatial variations in the density gradient^{8–12} can overcome the damping introduced by magnetic shear. Here, to obtain a theoretical description of the mode that is in reasonable agreement with the GS2 simulations for edgelike parameters, we go beyond past work and include in our analytic calculations the contributions from electron Landau damping, electromagnetic effects, as well as the spatial variation in the $\mathbf{E} \times \mathbf{B}$ velocity, density, and temperature profiles. This mode, due to its relatively large size (approaching the pedestal width itself) and its fairly robust linear growth rates even in the presence of $\mathbf{E} \times \mathbf{B}$ and magnetic shear, is a strong candidate for driving anomalous transport in the *H*-mode edge.

The analytic calculations we present are based on the Braginskii and gyrofluid models. These models are both “reduced,” in the sense that magnetosonic waves are assumed to be fast and are ordered out of the system. On the other hand, we also neglect the contribution of ion Landau damping and parallel sound waves. This assumption requires that $\partial_t \gg k_{\parallel} c_s$ for the modes of interest, where $c_s = \sqrt{(T_e + T_i)/m_i}$ is the sound speed. In the case of the Kelvin–Helmholtz mode,

for example, the typical *H*-mode edge parameters discussed later yield $\gamma_{\text{KH}}/(k_{\parallel} c_s) \sim c_A/c_s \sim 1/\sqrt{\beta} \gg 1$. This assumption also excludes the slab ITG mode from our analysis, as well as the parallel sheared-flow instability discussed by Cowley¹³ and shear damping effects due to ion-sound waves.¹⁴ In any case, as shown later the analytic results are in a good agreement with the GS2 simulations, in which the parallel ion dynamics are retained. The calculations also focus on modes that, at least marginally, satisfy $k_{\perp} \rho_i < 1$, so that an expansion in $k_{\perp}^2 \rho_i^2 \ll 1$ is justified. Finally, consistent with the remarks made earlier regarding diamagnetic effects, in the derivations we order the magnitude of the electron and ion diamagnetic flows to be comparable to the $\mathbf{E} \times \mathbf{B}$ flows. Given these assumptions, and working to leading order in $k_{\perp}^2 \rho_i^2$, we show that equivalent analytic results may be obtained from either the Braginskii or gyrofluid models. Calculations based on the Braginskii model are presented in the main text, while the (equivalent) gyrofluid calculations are described in Appendix B. We use the same electron model in both cases, which includes a simple approximation to electron Landau damping.

The GS2 simulations, as well as the analytic models, are based on the standard “flux-tube” ordering,¹⁵ in which the deviations of the absolute levels of the density and temperatures (for example) are assumed to be small over the region of interest, though deviations in the *gradients* of these quantities can be comparable to or larger than the equilibrium values. This assumption becomes marginal at best in the plasma edge, particularly in the case of the Kelvin–Helmholtz mode, which is expected to vary on the same scale as the equilibrium quantities. The quantitative study of such modes would therefore seem to require a fully nonlocal approach that goes beyond some of the calculations presented here.

This paper is organized as follows. We present the electron model that is used in the analytic calculations in Sec. II, the Braginskii ion model in Sec. III, and a set of reference edge parameters in Sec. IV. We then apply the results to the Kelvin–Helmholtz mode in Sec. V, the tertiary mode in Sec. VI, and the drift wave mode in Sec. VII. Section VIII contains a summary of the main findings in each case. In the appendixes, we discuss the validity of the adiabatic approximation (Appendix A), demonstrate the correspondence between the Braginskii and gyrofluid models (Appendix B), and analyze the role of shear in the case of the drift wave mode (Appendix C).

II. ELECTRON EQUATIONS

In this section we describe our electron model, and obtain a collection of important results that are used in the following sections. These results are independent of one’s choice of ion model, which is discussed in the following section.

The electron model we consider is given by

$$d_t n = \rho_s^2 \nabla_{\parallel} J, \quad (1)$$

$$\nabla_{\parallel} T_e = 0, \quad (2)$$

$$\alpha \partial_t \chi - \nabla_{\parallel}(\phi - n) = (\mu d_t + \nu + \lambda |k_{\parallel}|)J, \quad (3)$$

where

$$J = \nabla_{\perp}^2 \chi, \quad \nabla_{\parallel} = \partial_z + \alpha \hat{z} \times \nabla_{\perp} \chi \cdot \nabla_{\perp}, \quad (4)$$

$$d_t = \partial_t + \hat{z} \times \nabla_{\perp} \phi \cdot \nabla_{\perp}, \quad \nabla_{\perp} = \hat{x} \partial_x + \hat{y} \partial_y, \quad (5)$$

$$\alpha = \left(\frac{L_{\parallel}}{c_A t_0} \right)^2, \quad \rho_s = \frac{\rho_{se}}{L_{\perp}}, \quad \mu = \alpha \frac{d_e^2}{L_{\perp}^2}, \quad (6)$$

$$\lambda = \mu \sqrt{\frac{\pi \nu_{the} t_0}{2 L_{\parallel}}}, \quad \nu = \mu \nu_{ei} t_0, \quad (7)$$

$$\rho_{se} = \frac{c_{se}}{\omega_{ci}}, \quad d_e = \frac{c}{\omega_{pe}}, \quad d_i = \frac{c}{\omega_{pi}}, \quad (8)$$

$$\omega_{ci} = \frac{e B_0}{m_i c}, \quad \omega_{pe}^2 = \frac{4 \pi n_0 e^2}{m_e}, \quad (9)$$

$$c_{se}^2 = \frac{T_{e0}}{m_i}, \quad \nu_{the}^2 = \frac{T_{e0}}{m_e}, \quad c_A^2 = \frac{B_0^2}{4 \pi n_0 m_i}, \quad (10)$$

$$(t, \nabla_{\perp}, \nabla_{\parallel}) = \left(\frac{t_{phys}}{t_0}, L_{\perp} \nabla_{\perp, phys}, L_{\parallel} \nabla_{\parallel, phys} \right), \quad (11)$$

$$(n, T_e) = \left(\frac{n_{e, phys}}{n_0}, \frac{T_{e, phys}}{T_{e0}} \right) \frac{t_0 c_{se} \rho_{se}}{L_{\perp}^2}, \quad (12)$$

$$(\phi, \chi) = \left(\frac{c t_0 \phi_{phys}}{L_{\perp}^2 B_0}, -\frac{t_0^2 c_A^2 A_{z, phys}}{L_{\perp}^2 L_{\parallel} B_0} \right), \quad (13)$$

$$\vec{B}_{phys} = -\hat{z} \times \nabla_{\perp} A_{z, phys} + B_0 \hat{z}. \quad (14)$$

The term proportional to λ in Eq. (3) represents a simple approximation to electron Landau damping,¹⁶ the ν term represents electron-ion collisions, and the μd_t term arises from electron inertia. Note that, for later flexibility, we have written the normalized equations in terms of arbitrary time and length scales t_0 , L_{\perp} , L_{\parallel} . These can be chosen to suit the particular problem or mode under consideration. For example, when comparing to the GS2 simulations in the following sections, we choose $L_{\perp} = \rho_{se}$, $L_{\parallel} = R$, $t_0 = R/c_{se}$, in which case

$$\rho_s = 1, \quad \alpha = \frac{\beta_e}{2} = \frac{4 \pi n_0 T_{e0}}{B_0^2}, \quad (15)$$

$$\mu = \frac{m_e}{m_i}, \quad \nu = \frac{m_e \nu_{ei} R}{m_i c_{se}}, \quad \lambda = \sqrt{\frac{\pi m_e}{2 m_i}}. \quad (16)$$

The parameter R , usually associated with the radius of curvature, is introduced here only as a convenient parallel normalization scale. It has no physical meaning in the present slab system and, when our results are written in non-normalized units, it necessarily drops out.

Finally, we note the assumption of an isothermal electron response made in Eq. (2) can be physically marginal in some

cases of interest. For example, $k_{\parallel} \nu_{the}$ can approach the growth rates of some of the faster modes of interest here, and in the more collisional edge plasma of Alcator C-Mod, for example, the electron mean-free path can approach the parallel connection length ($\lambda_{mfp} \sim qR$). This issue is further underscored by the GS2 simulations, which in the case of the drift wave mode, for example, exhibit a weak stabilizing dependence on the equilibrium electron temperature gradient that is not properly reproduced by Eq. (2). In any case, here we will use Eq. (2) and leave the detailed study of electron temperature gradient effects for future work.

We now separate the various quantities into an ‘‘equilibrium’’ part, assumed to depend only on x , and a perturbation. For any quantity f ,

$$f = f_0(x) + \tilde{f}(x) e^{\gamma t + i k_y y + i k_z z}, \quad (17)$$

$$d_t f = \bar{\gamma} \tilde{f} - i k_y f_0' \tilde{\phi}, \quad \bar{\gamma} = \gamma + i k_y \phi_0', \quad (18)$$

$$\nabla_{\parallel} f = i k_{\parallel} \tilde{f} - i \alpha k_y f_0' \tilde{\chi}, \quad k_{\parallel} = k_z + \alpha k_y \chi_0', \quad (19)$$

$$\nabla_{\parallel} J = i k_{\parallel} \nabla_{\perp}^2 \tilde{\chi} - i k_{\parallel}'' \tilde{\chi} = i \partial_x [k_{\parallel}^2 \partial_x (\tilde{\chi}/k_{\parallel})] - i k_y^2 k_{\parallel} \tilde{\chi}. \quad (20)$$

As an example, in the particular case of constant magnetic shear considered later,

$$\vec{B}_{0, phys} = B_0 \left(\hat{e}_z + \frac{x_{phys}}{L_s} \hat{e}_y \right), \quad (21)$$

$$k_{\parallel} = \frac{L_{\parallel}}{L_s} (k_{z, phys} L_s + k_y x). \quad (22)$$

Due to the form of Ohm’s law [Eq. (3)], it turns out to be most convenient to work in terms of the variable $\phi - n$, the so-called nonadiabatic response. We therefore define

$$\tilde{\phi}_e = \tilde{\phi} - \tilde{n}, \quad \bar{\gamma}_e = \gamma + i k_y (\phi_0' - n_0'). \quad (23)$$

Here $\bar{\gamma}_e$ is the (complex) growth rate in a frame drifting with the electrons, while $\bar{\gamma}$ [see Eq. (18)] is the growth rate in a frame drifting with the $\mathbf{E} \times \mathbf{B}$ velocity. Using Eq. (1), one can express \tilde{n} and $\tilde{\phi}$ in terms of $\tilde{\phi}_e$ and $\nabla_{\parallel} J$ as

$$\tilde{n} = \frac{1}{\bar{\gamma}} (i k_y n_0' \tilde{\phi} + \rho_s^2 \nabla_{\parallel} J) = \frac{1}{\bar{\gamma}_e} (i k_y n_0' \tilde{\phi}_e + \rho_s^2 \nabla_{\parallel} J), \quad (24)$$

$$\tilde{\phi} = \tilde{\phi}_e + \tilde{n} = \frac{1}{\bar{\gamma}_e} (\bar{\gamma} \tilde{\phi}_e + \rho_s^2 \nabla_{\parallel} J). \quad (25)$$

For later use in the study of the tertiary mode, note that in the adiabatic limit ($\alpha \rightarrow 0$, $\mu \rightarrow 0$, $\nu \rightarrow 0$, $\lambda \rightarrow 0$),

$$\tilde{\phi}_e = 0 + \dots, \quad (26)$$

$$\tilde{\phi} = \tilde{n} = \frac{\rho_s^2 \nabla_{\parallel} J}{\bar{\gamma}_e}. \quad (27)$$

The condition under which this approximation becomes valid is discussed in Appendix A, and is given by Eq. (A4).

The final step in this section is to relate $\tilde{\chi}$ to $\tilde{\phi}_e$ using Ohm’s law [Eq. (3)]. Here we slightly simplify the final re-

sult by dropping some terms proportional to $\mu J'_0$, that is, electron inertia terms associated with the background current gradient. These terms, which vanish anyway for the case of constant magnetic shear, will not play a role in any of our subsequent analyses. Dropping such terms, one obtains

$$\alpha \bar{\gamma}_e \bar{\chi} - (\mu \bar{\gamma} + \nu + \lambda |k_{\parallel}|) \nabla_{\perp}^2 \bar{\chi} = ik_{\parallel} \bar{\phi}_e. \quad (28)$$

For later use in the study of the Kelvin–Helmholtz mode, note that in the “ideal” limit of $\mu \rightarrow 0$, $\nu \rightarrow 0$, $\lambda \rightarrow 0$:

$$\bar{\chi} = \frac{ik_{\parallel} \bar{\phi}_e}{\alpha \bar{\gamma}_e}. \quad (29)$$

Using this to eliminate $\bar{\chi}$ in Eq. (20) then gives

$$\nabla_{\parallel} J = \frac{1}{\alpha} \{-\partial_x [k_{\parallel}^2 \partial_x (\bar{\phi}_e / \bar{\gamma}_e)] + k_y^2 k_{\parallel}^2 \bar{\phi}_e / \bar{\gamma}_e\}. \quad (30)$$

This expression is valid for any profile of k_{\parallel} (that is, χ'_0).

III. BRAGINSKII ION MODEL

To make further progress, it is necessary to supplement these results with another equation relating $\bar{\chi}$ to $\bar{\phi}_e$. Such an equation is now obtained by introducing an ion model. As discussed in the Introduction, we describe here a Braginskii model, although equivalent results may be obtained to the order we are working from gyrofluid calculations that are described in Appendix B.

The Braginskii model we consider is given by¹⁷

$$\nabla_{\perp} \cdot d_t \nabla_{\perp} (\phi + \tau p_i) = \nabla_{\parallel} J, \quad (31)$$

$$d_t T_i = 0, \quad (32)$$

$$p_i = n + T_i, \quad \tau = T_{i0} / T_{e0}, \quad (33)$$

$$d_t p_i = \rho_s^2 \nabla_{\parallel} J, \quad (34)$$

$$(p_i, T_i) = \left(\frac{p_{i,\text{phys}}}{p_{i0}}, \frac{T_{i,\text{phys}}}{T_{i0}} \right) \frac{t_0 c_{se} \rho_{se}}{L_{\perp}^2}. \quad (35)$$

Note we have chosen here an isothermal ion equation of state. This choice is necessary to obtain agreement with the gyrofluid model calculations discussed in the appendixes. The gyrofluid calculations also make it apparent that the perturbations p_i , T_i appearing above are in fact $p_{i\perp}$, $T_{i\perp}$. The contributions from $p_{i\parallel}$, $T_{i\parallel}$ do not enter our system due to our neglect of the parallel sound wave dynamics.

Linearizing these equations as discussed in the last section, Eq. (34) gives

$$\bar{p}_i = \frac{1}{\bar{\gamma}} (ik_y p'_{i0} \bar{\phi} + \rho_s^2 \nabla_{\parallel} J). \quad (36)$$

Then defining $\bar{\gamma}_i$ (γ shifted into the ion frame) as

$$\bar{\gamma}_i = \gamma + ik_y (\phi'_0 + \tau p'_{i0}) \quad (37)$$

and using Eqs. (25) and (36), one finds

$$\bar{\phi}_i = \bar{\phi} + \tau \bar{p}_i = \frac{1}{\bar{\gamma}_i} (\bar{\gamma}_i \bar{\phi} + \tau \rho_s^2 \nabla_{\parallel} J) \quad (38)$$

$$= \frac{1}{\bar{\gamma}_e} \left(\bar{\gamma}_i \bar{\phi}_e + \frac{\bar{\gamma}_i + \tau \bar{\gamma}_e}{\bar{\gamma}} \rho_s^2 \nabla_{\parallel} J \right). \quad (39)$$

Solving Eq. (38) for $\bar{\phi}$ in terms of $\bar{\phi}_i$ and substituting the result into the vorticity equation [Eq. (31)] gives

$$\partial_x \left[\bar{\gamma} \bar{\gamma}_i \partial_x \left(\frac{\bar{\phi}_i}{\bar{\gamma}_i} \right) + \frac{\tau \bar{\gamma}'_i}{\bar{\gamma}_i} \rho_s^2 \nabla_{\parallel} J \right] = k_y^2 \bar{\gamma} \bar{\phi}_i + \nabla_{\parallel} J. \quad (40)$$

Equivalently, eliminating $\bar{\phi}_i$ with Eq. (39), this result can be written as

$$\partial_x \left[\bar{\gamma} \bar{\gamma}_i \partial_x \left(\frac{\bar{\phi}_e}{\bar{\gamma}_e} \right) \right] - k_y^2 \bar{\gamma} \bar{\gamma}_i \frac{\bar{\phi}_e}{\bar{\gamma}_e} = F_{\parallel}, \quad (41)$$

$$F_{\parallel} = \nabla_{\parallel} J - \partial_x \left(\tau \bar{\gamma}'_e \frac{\rho_s^2 \nabla_{\parallel} J}{\bar{\gamma}_e} \right) - \partial_x \left[\bar{\gamma} (\bar{\gamma}_i + \tau \bar{\gamma}_e) \partial_x \left(\frac{\rho_s^2 \nabla_{\parallel} J}{\bar{\gamma} \bar{\gamma}_e} \right) \right] + k_y^2 (\bar{\gamma}_i + \tau \bar{\gamma}_e) \frac{\rho_s^2 \nabla_{\parallel} J}{\bar{\gamma}_e}. \quad (42)$$

This is the desired final result relating $\bar{\chi}$ to $\bar{\phi}_e$. Using Eqs. (20) and (28) to eliminate $\nabla_{\parallel} J$ and $\bar{\phi}_e$ from Eq. (41), for example, one obtains a single fourth-order eigenvalue equation for $\bar{\chi}$. This equation describes several distinct instabilities that are discussed in the following sections. Reconnection modes, though included in the formalism at this point, will not be discussed here.

As a final point, we note these eigenvalue equations possess a self-similar family of solutions given by the scaling $\gamma \rightarrow \Lambda \gamma$, $\phi'_0 \rightarrow \Lambda \phi'_0$, $n'_0 \rightarrow \Lambda n'_0$, $p'_{i0} \rightarrow \Lambda p'_{i0}$, $k_{\parallel} \rightarrow \Lambda k_{\parallel}$, $\nu \rightarrow \Lambda \nu$, where Λ is a constant. As a result, as the flows represented by ϕ'_0 , n'_0 , etc., are made stronger, the contributions from ν (the collisionality) and k_{\parallel} will generally become weaker if these quantities are held fixed. On the other hand, for modes that *require* finite k_{\parallel} (such as the tertiary mode or the drift wave), the unstable values of k_{\parallel} must also increase in proportion to the strength of the flows. This feature has been verified numerically by the GS2 simulations.

IV. REFERENCE PARAMETERS AND GS2 SETUP

In the following sections, we will refer to some sample parameters taken from the literature that roughly characterize the *H*-mode edge pedestal regions in two tokamaks, DIII-D (Ref. 18) and Alcator C-MOD.¹⁹ DIII-D: $R \approx 168$ cm, $n \sim 2 \times 10^{13}$ cm⁻³, $m_i = 2m_p$, $T_e \sim T_i \sim 350$ eV, $B \sim 2$ T, $\beta_e \sim 7.1 \times 10^{-4}$, $\rho_{se} \sim 0.13$ cm, $d_e \sim 0.12$ cm, $d_i \sim 7.2$ cm, $\hat{s} \sim 2$, $q \sim 3.5$, $\lambda_{mfip}/qR \sim 10$, $c_s \sim 1.8 \times 10^5$ m/s. Alcator C-MOD: $R \approx 68$ cm, $n \sim 1.5 \times 10^{14}$ cm⁻³, $m_i = 2m_p$, $T_e \sim T_i \sim 250$ eV, $B \sim 5.3$ T, $\beta_e \sim 5.4 \times 10^{-4}$, $\rho_{se} \sim 0.043$ cm, $d_e \sim 0.043$ cm, $d_i \sim 2.6$ cm, $\hat{s} \sim 2$, $q \sim 3.5$, $\lambda_{mfip}/qR \sim 2$, $c_s \sim 1.5 \times 10^5$ m/s.

As noted earlier, comparisons to the GS2 code will utilize the normalization given by Eqs. (15) and (16). In this normalization, the ordering $V_E \sim V_{*e}$ discussed in the Introduction is equivalent to $\phi \sim R/\rho_{se}$, or in either of the two cases given above, $\phi \sim 1.5 \times 10^3$. Given that $V_E = \phi' \sim \phi/\delta$ where $\delta \sim 5$ ($=5\rho_{se}$) is a “typical” pedestal half width in either case, one obtains $V_E \sim -V_{*i} \sim 300$ in normalized units. The magnetic shear model in the GS2 simulations is given

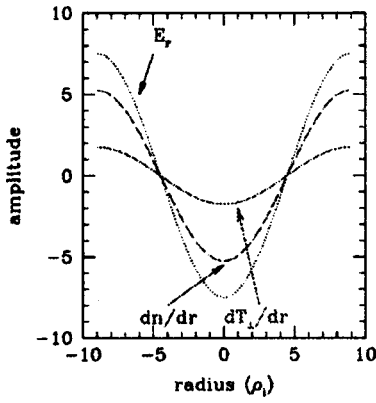


FIG. 1. Typical GS2 simulation profiles, corresponding to a “periodic barrier.”

by Eq. (21) with $L_s = qR/\hat{s}$. Due to the radially periodic boundary conditions in the GS2 code, the simulations we present are based on a simple periodic slab geometry with no curvature,

$$\begin{aligned}\phi'_0 &= V_E \cos(k_x x), \\ \pi n'_0 &= V_{*in} \cos(k_x x), \\ \tau T'_{i0} &= V_{*iT} \cos(k_x x), \\ \tau p'_{i0} &= V_{*i} \cos(k_x x), \quad V_{*i} = V_{*in} + V_{*iT}.\end{aligned}\quad (43)$$

As noted earlier, here $T'_{i0} = T'_{i0\perp}$, $p'_{i0} = p'_{i0\perp}$; for simplicity we take $T'_{i0\parallel} = p'_{i0\parallel} = 0$. A typical example is shown in Fig. 1. Because the tertiary and drift wave eigenmodes are spatially localized to the regions where the plasma gradients are steepest, these modes depend on the structure of the profiles only in a small region, and are not sensitive, for example, to the periodic or nonperiodic nature of the profiles or boundary conditions away from the peak-gradient region. It is less obvious that this insensitivity would apply to the Kelvin–Helmholtz mode, which has a more global mode structure. However, we present analytic calculations of both periodic and nonperiodic profiles for this mode as well and show that the results are indeed qualitatively similar.

V. KELVIN–HELMHOLTZ INSTABILITY

The standard Kelvin–Helmholtz instability, modified by diamagnetic and electromagnetic effects, may be conveniently obtained from Eq. (41) in the limit that the nonideal terms on the right-hand side of Ohm’s law proportional to μ , ν , λ are neglected and we consider $k_\perp^2 \rho_s^2 \ll 1$. Dropping terms of $O(k_\perp^2 \rho_s^2)$ compared to unity in Eq. (42), F_\parallel reduces to $F_\parallel \approx \nabla_\parallel J$. Then using the expression for $\nabla_\parallel J$ given by Eq. (30) in Eq. (41), one obtains

$$\partial_x \left[\left(\bar{\gamma} \bar{\gamma}_i + \frac{k_\parallel^2}{\alpha} \right) \partial_x \xi \right] = k_y^2 \left(\bar{\gamma} \bar{\gamma}_i + \frac{k_\parallel^2}{\alpha} \right) \xi, \quad (44)$$

where

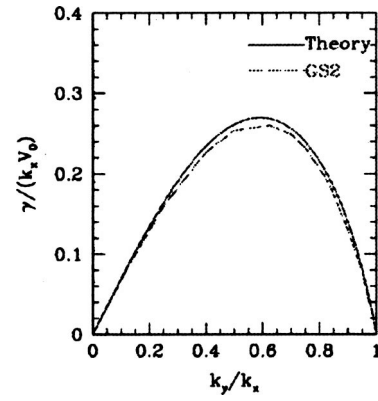


FIG. 2. KH mode γ vs k_y/k_x .

$$\bar{\xi} = \frac{\bar{\phi}_e}{\bar{\gamma}_e} \approx \frac{\bar{\phi}_i}{\bar{\gamma}_i} \approx \frac{\bar{\phi}}{\bar{\gamma}} \quad (k_\perp^2 \rho_s^2 \ll 1). \quad (45)$$

The Kelvin–Helmholtz instability described by Eq. (44) can be stabilized by either ion diamagnetic effects or magnetic shear (line bending). To illustrate this, we now consider two simple models, one periodic and one nonperiodic. In the periodic case, an analytic form of the dispersion relation may be obtained in the long-wavelength limit $k_y^2 L^2 \ll 1$, where L is typical scale length of the equilibrium variation, for example, $L^2 \sim |\phi'_0/\phi''_0|$. Given $k_y^2 L^2 \ll 1$, the terms on the right-hand side of Eq. (44) are small, and the leading-order solution is $\xi \approx \text{const}$. The leading order dispersion relation may then be obtained by integrating Eq. (44) over one period in x , which annihilates the left-hand side. The result, given $\xi \approx \text{const}$, is the dispersion relation

$$\left\langle \bar{\gamma} \bar{\gamma}_i + \frac{k_\parallel^2}{\alpha} \right\rangle = 0, \quad (46)$$

where $\langle \dots \rangle$ denotes the integral over one period. As an example, consider

$$\phi'_0 = V_E \cos(k_x x), \quad (47)$$

$$\tau p'_{i0} = V_{*i} \cos(k_x x), \quad (48)$$

$$\chi'_0 = B_y \cos(k_x x), \quad (49)$$

$$\bar{\gamma} = \gamma + ik_y V_E \cos(k_x x), \quad (50)$$

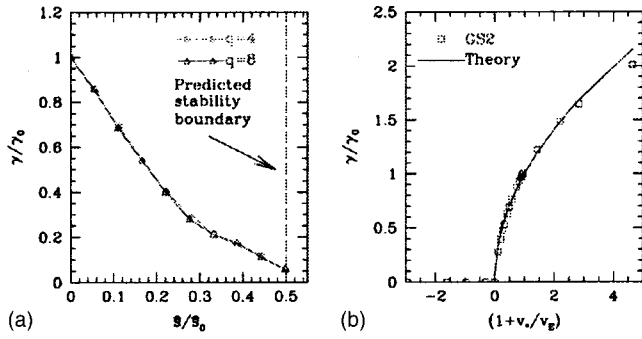
$$\bar{\gamma}_i = \gamma + ik_y V_{*i0} + ik_y (V_E + V_{*i}) \cos(k_x x), \quad (51)$$

$$k_\parallel = k_z + \alpha k_y B_y \cos(k_x x), \quad (52)$$

which leads to the dispersion relation (for $k_y^2 \ll k_x^2$)

$$\gamma(\gamma + ik_y V_{*i0}) = \frac{1}{2} k_y^2 [V_E (V_E + V_{*i}) - \alpha B_y^2] - \frac{k_z^2}{\alpha}. \quad (53)$$

The exact numerical solution of Eq. (44) in the case with $k_\parallel = 0$ and $V_{*i} = V_{*i0} = 0$, along with the corresponding GS2 simulation values, is shown in Fig. 2, where we plot $\gamma/(k_x V_E)$ versus k_y/k_x (other parameters in the GS2 simulations are $k_y \rho_s = 0.2$, $T_i = T_e$, $\hat{s} = 0$, $\beta_e = 10^{-4}$). Consistent with

FIG. 3. KH mode γ vs (a) \hat{s}/\hat{s}_0 and (b) V_{*i} .

Eq. (53), $\gamma = k_y V_E / \sqrt{2}$ at $k_y \ll k_x$. The maximum growth rate is $\gamma = 0.27 k_x V_E$ for $k_y = 0.59 k_x$. The frequency $[\text{Im}(\gamma)]$ in this case is zero.

Returning to Eq. (46) it is clear that finite k_{\parallel} (that is, finite B_y and/or k_z) is stabilizing. The threshold for stabilization is $k_{\parallel} \sim \sqrt{\alpha} \gamma_{\text{KH}} \sim \sqrt{\alpha} V_E / L$ or in physical units,

$$k_{\parallel, \text{phys}} \sim \frac{V_E}{c_A L}. \quad (54)$$

Assuming $k_{\parallel, \text{phys}} \sim k_y x / L_s \sim 1 / L_s$, this gives

$$L_s \sim \frac{c_A L}{V_E} \sim \frac{c_A}{V_{E, \text{max}}}. \quad (55)$$

Figure 3(a) shows the comparison of this condition with GS2 simulations for the case of a sinusoidal $\mathbf{E} \times \mathbf{B}$ flow profile and constant magnetic shear [see Eqs. (21) and (22)]. As in a tokamak, we parametrize the shear length L_s in terms of the parameter \hat{s} as $L_s = qR / \hat{s}$, and γ_0 is the growth rate for $\hat{s} = 0$. The other GS2 simulation parameters are $k_x \rho_i = 0.2$, $T_i = T_e$, $\phi_0 = 2 \times 10^3$, and $\beta_e = 10^{-4}$. Motivated by Eq. (55), on the lower axis we plot the data as a function of the dimensionless parameter,

$$\frac{c_A}{L_s V_{E, \text{max}}} \equiv \frac{\hat{s}}{\hat{s}_0}, \quad \hat{s}_0 = \frac{q R V_{E, \text{max}}'}{c_A} \quad (56)$$

(or in the GS2 units discussed earlier $\hat{s}_0 = q k_x^2 \sqrt{\beta_e / 2} \phi_0$). As a demonstration of the predicted \hat{s}_0 scaling, we show the results for two different q values: $q = 4$ and $q = 8$. Stability is reached at $\hat{s} = 0.51 \hat{s}_0$, or evaluating \hat{s}_0 with the parameters of Sec. IV (one finds $\hat{s}_0 = 4.0$ for DIII-D and $\hat{s}_0 = 3.5$ for C-MOD), $\hat{s} \approx 2$. Stabilization of the KH mode due to shear in this simple model is therefore reached at a value of \hat{s} that is typical of the edge. A similar finding is obtained below in the case of a more realistic nonperiodic velocity shear profile.

Turning now to the role of ion diamagnetic effects, one can see from Eq. (53) that either a spatially constant or spatially varying ion diamagnetic flow (represented by V_{*i0} and V_{*i} , respectively) can also stabilize the mode. Denoting the right-hand side of Eq. (53) by Γ_0^2 (Γ_0 therefore being the growth rate of the mode when $V_{*i0} = 0$), one finds that instability requires

$$\Gamma_0 > |k_y V_{*i0}| / 2. \quad (57)$$

One can also see from Eq. (53) that

$$V_E (V_E + V_{*i}) > 0 \quad (58)$$

is a necessary condition for instability. This condition may also be obtained in the general periodic or nonperiodic case by multiplying Eq. (44) by ξ^* , integrating over the domain of the mode, integrating the left-hand side by parts, and solving for γ . One finds that Eq. (58) (with V_{*i} interpreted as the total ion diamagnetic velocity) must be satisfied *somewhere* within the envelope of the mode in order for instability to be possible. In the most unstable case of $k_{\parallel} = 0$, therefore, the mode will be stable if V_{*i} is in the opposite direction to V_E and at least equal in magnitude. Consistent with this, the numerical solution of Eq. (44) as well as the GS2 simulations both predict stability of the Kelvin–Helmholtz mode when Eq. (58) is not satisfied. This is demonstrated in Fig. 3(b), which shows γ / γ_0 (the growth rate normalized to its value with $V_{*i} = 0$) versus $(1 + V_{*i} / V_E)$ [Eq. (58) divided by V_E^2] in the case of $\hat{s} = 0$ and $V_{*i0} = 0$. Since one expects $V_{*i} / V_E \sim -1$ for the H -mode pedestal as discussed earlier, it would seem that diamagnetic effects, like magnetic shear, may also stabilize or nearly stabilize the Kelvin–Helmholtz mode for typical edge conditions.

To illustrate the effects of magnetic shear in a more realistic velocity profile, we now consider a simple nonperiodic pedestal model with a constant magnetic shear [see Eqs. (21) and (22)] and, for simplicity, no ion diamagnetic effects,

$$\phi_0 = V_E \delta \tanh(x / \delta), \quad (59)$$

$$\phi_0' = V_y = V_E \{1 - [\tanh(x / \delta)]^2\}, \quad (60)$$

$$p_i = 0; \quad (61)$$

or choosing the normalization $L_{\perp} = \delta$, $t_0 = \delta / V_E$, $L_{\parallel} = L_s$,

$$\phi_0 = \tanh(x), \quad (62)$$

$$\phi_0' = V_y = 1 - [\tanh(x)]^2, \quad (63)$$

$$p_i = 0, \quad (64)$$

$$k_{\parallel} = k_{z, \text{phys}} L_s + k_y x, \quad (65)$$

$$\alpha = \left(\frac{V_E L_s}{c_A \delta} \right)^2. \quad (66)$$

For $\alpha \rightarrow \infty$, the fastest growing mode has $\gamma_{\text{phys}} = (0.16, -0.41) V_E / \delta$ for $k_{y, \text{phys}} \delta = 0.9$. Overall stability is reached at $\alpha \approx 2$ (where the marginally stable mode has $k_{y, \text{phys}} \delta \approx 1.4$, $k_{z, \text{phys}} L_s \approx 0.7$). Note that the condition $\alpha \sim 2$, given Eq. (66), and $\delta \sim L$ is consistent with Eq. (55). Upon taking $L_s = qR / \hat{s}$ as in a tokamak, and defining a normalized $\mathbf{E} \times \mathbf{B}$ flow velocity $V_{E, N} \equiv (V_E / v_{\text{thi}})(\delta / \rho_i)$ (so that $V_{E, N} \sim 1$) one finds

$$\alpha = \left(\frac{V_E L_s}{c_A \delta} \right)^2 = \left(\frac{\rho_i^2 q R}{\delta^2 d_i \hat{s}} V_{E, N} \right)^2, \quad (67)$$

where $d_i = c / \omega_{pi}$ is the ion skin depth. Thus, the condition for stability $\alpha \lesssim 2$ gives

$$\delta \geq 0.8\rho_i \left(\frac{qR}{d_i \hat{s}} V_{E,N} \right)^{1/2}. \quad (68)$$

For a fixed level of V_E and magnetic shear, the mode therefore becomes unstable when the pedestal is sufficiently narrow. Including ion diamagnetic effects, one obtains a similar estimate with the replacement $V_E \rightarrow \sqrt{V_E(V_E + V_{*i})}$.

Evaluating Eq. (68) for the sample H -mode edge parameters given in Sec. IV, and assuming $V_{E,N} \sim 1$, we obtain a marginally stable value of $\delta \sim 5\rho_i$ for either DIII-D or Alcator C-Mod. Given that δ here is the characteristic pedestal scale length and is thus about half the total pedestal width, this estimate is close to the value observed in the experiments. An accurate assessment of the importance of this mode in the H -mode edge therefore requires a careful account of both magnetic shear and ion diamagnetic effects. With respect to internal transport barriers, which are characterized by strong sheared flows and very weak magnetic shear, the general absence of the KH mode is likely due in part to diamagnetic stabilization.

VI. TERTIARY MODE

In contrast to the Kelvin–Helmholtz mode, which is most unstable for $k_{\parallel} \rightarrow 0$, the tertiary mode² may be obtained from Eq. (41) by considering the limit of high k_{\parallel} in which the adiabatic approximation given by Eqs. (26) and (27) becomes valid: $\tilde{\phi}_e = 0$ and $\rho_s^2 \nabla_{\parallel} J = \tilde{\gamma}_e \tilde{\phi}$. Applying these to Eq. (41), one obtains

$$\partial_x \left[\tilde{\gamma} (\tilde{\gamma}_i + \tau \tilde{\gamma}_e) \partial_x \left(\frac{\tilde{\phi}}{\tilde{\gamma}} \right) + \tau \tilde{\gamma}_e \tilde{\phi} \right] = \left[\frac{\tilde{\gamma}_e}{\rho_s^2} + k_y^2 (\tilde{\gamma}_i + \tau \tilde{\gamma}_e) \right] \tilde{\phi}. \quad (69)$$

The tertiary instability is an eigenmode of this equation which is driven by the ion temperature gradient T'_{i0} and is spatially localized by the $\mathbf{E} \times \mathbf{B}$ shear profile. As is the case in the edge pedestal, we assume that $\phi'_0 \propto V_E$ takes on some positive maximum value at a location where $T'_0 < 0$, so that

$$T'_0 \phi_0''' > 0. \quad (70)$$

To make further analytic progress with Eq. (69), we will assume that the temperature gradient satisfies the ordering $\tau T'_{i0} \sim \phi'_0$, or in physical units, $V_{*i,T} \sim \rho_i V_{\text{thi}}/L_T \sim V_E$, where $L_T \sim T_{i0}/T'_{i0}$ is the ion temperature scale length. We also assume, for reasons explained later, that $L_T < L_n$ where $L_n \sim n_0/n'_0$, so that $\eta_i = L_n/L_T > 1$. Finally, we utilize the fact that $L^2 \gg \rho_s^2$ where L is the equilibrium scale. With these assumptions, the tertiary mode turns out to have an x -scale length $\Delta_t \sim \sqrt{L\rho_s}$ that is large compared to ρ_s but small compared to L . This allows us to expand ϕ'_0 about its maximum, taken to be at $x=0$:

$$\phi'_0(x) = \phi'_0(0) + \phi_0'''(0)x^2/2 + \dots \quad (71)$$

[The quantities n'_0 and T'_0 can be similarly expanded, but given the assumptions just outlined, the higher order contributions to these quantities do not enter the final result, so that one can take $n'_0 \approx n'_0(0)$ and $T'_{i0} \approx T'_{i0}(0)$.] Expanding the

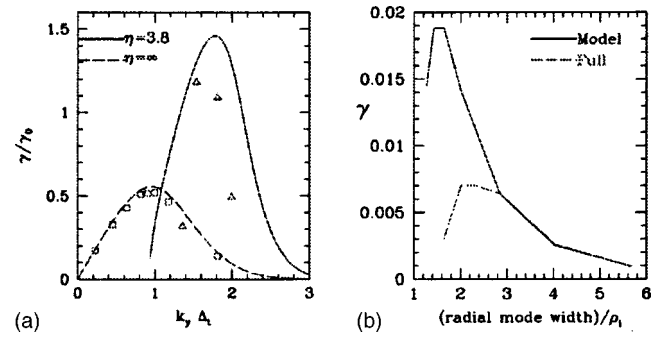


FIG. 4. Tertiary mode γ vs (a) k_y for $\eta_i = \infty$ (squares), $\eta_i = 3.8$ (triangles), and (b) Δ_t .

equilibrium quantities in Eq. (69) as in Eq. (71), introducing the normalized variables

$$\hat{x} = \frac{x}{\Delta_t}, \quad \hat{k}_y = k_y \Delta_t, \quad \Gamma = \hat{\gamma} - i \hat{k}_y \hat{x}^2, \quad (72)$$

$$\hat{\gamma} = \frac{\gamma + i k_y \phi'_0(0)}{\gamma_0}, \quad \gamma_0 = \frac{1}{2} \Delta_t |\phi_0'''(0)|, \quad (73)$$

$$\Delta_t = \left(\frac{2\tau\rho_s^2 T'_{i0}(0)}{\phi_0'''(0)} \right)^{1/4} \sim \sqrt{L\rho_s}, \quad (74)$$

and assuming $k_y^2 \rho_s^2 \ll 1$, one obtains the leading order terms

$$\partial_{\hat{x}} \left[\Gamma \partial_{\hat{x}} \left(\frac{\tilde{\phi}}{\Gamma} \right) \right] = \left(\frac{i\Gamma}{\hat{k}_y} + \hat{k}_y^2 - C_n \right) \tilde{\phi}, \quad (75)$$

$$C_n = \frac{\Delta_t^2 n'_0(0)}{\tau\rho_s^2 T'_{i0}(0)}. \quad (76)$$

We begin the analysis of Eq. (75) by considering the case of $C_n \approx n'_0 = 0$. In this case, a unique result for $\hat{\gamma}(\hat{k}_y)$ may be obtained by solving Eq. (75) numerically. The result for $\hat{\gamma}_r = \text{Re}(\hat{\gamma}) = \text{Re}(\gamma)/\gamma_0$ versus \hat{k}_y is shown in Fig. 4(a) (dashed line), and is seen to agree well with the GS2 results (squares, obtained with $k_x \rho_i = 0.2$, $T_i = T_e$). The fastest growing mode occurs for $\hat{k}_y (= k_y \Delta_t) = 0.96$ and has $\hat{\gamma} \approx 0.56 + 1.44i$. For $\hat{k}_y \ll 1$, $\hat{\gamma} \approx (0.80 + 0.84i)\hat{k}_y$. Thus

$$\text{Re}(\gamma) \sim \gamma_0 = \frac{1}{2} \Delta_t |\phi_0'''(0)| \sim \sqrt{\frac{\rho_s V_E}{L}}, \quad (77)$$

$$\text{Im}(\gamma) \approx -k_y \phi'_0(0) \left[1 + O\left(\sqrt{\frac{\rho_s}{L}} \right) \right] \approx -k_y V_E. \quad (78)$$

The mode is seen to drift with the local $\mathbf{E} \times \mathbf{B}$ velocity and have a growth rate that is weaker than the typical Kelvin–Helmholtz value $\gamma_{\text{KH}} \sim V_E/L$ by a factor of $\sqrt{\rho_s/L}$ (only a modest reduction for typical pedestals, in which $\sqrt{\rho_s/L} \sim 1/3 - 1/2$).

Turning to the case with finite n'_0 ($C_n \neq 0$), the growth rate $[\text{Re}(\hat{\gamma})]$ for the value $C_n = 3.8$ is shown in Fig. 4(a). The solid line is the solution of Eq. (75) and the triangles are the GS2 values obtained with $k_x \rho_i = 0.2$, $T_i = T_e$. (The agreement

between the two is not as good for these parameters due to the stabilizing contribution of FLR effects in the GS2 simulations.) As is the case for any $C_n \geq 1$, the maximum growth rate occurs at the wave number $\hat{k}_y \approx \sqrt{C_n}$ where the last two terms on the right-hand side of Eq. (75) almost cancel. Dropping these terms, the form of Eq. (75) becomes identical to the previous $C_n=0$ case in the limit $\hat{k}_y \ll 1$, in which $\hat{\gamma} \approx (0.80+0.84i)\hat{k}_y$. Thus, for $C_n \geq 1$, the peak growth rate has $\hat{k}_y \approx \sqrt{C_n}$ and $\hat{\gamma} \approx (0.80+0.84i)\sqrt{C_n}$. In physical units, the condition $\hat{k}_y \approx \sqrt{C_n}$ is equivalent to

$$k_y^2 \rho_i^2 \approx \left(\frac{n'_0 T'_{i0}}{n_0 T'_{i0}} \right)_{x=0} \equiv \frac{1}{\eta_i}, \quad (79)$$

which is consistent with the restriction $k_y^2 \rho_i^2 \ll 1$ if $\eta_i > 1$, as assumed earlier. In addition, the growth rate can be written as

$$\text{Re}(\gamma) \approx 0.80 k_y \Delta_i \gamma_0 \approx 0.80 \sqrt{n'_0(0) \phi''_0(0)}/2. \quad (80)$$

Thus, despite the T'_{i0} dependence of k_y , the peak growth rate does not depend on the temperature gradient in this case.

As noted in the Introduction, according to the GS2 simulations, the tertiary mode can be stabilized by finite Larmor radius effects when the pedestal scale length becomes sufficiently narrow. This is shown in Fig. 4(b), which is a plot of the growth rate of the mode versus the radial mode width Δ_i/ρ_i . Stabilizing FLR contributions lead to a significant reduction of the GS2 growth rate relative to the lowest order theory in this case when $\Delta_i \lesssim 3\rho_i$, which (for the parameters of the simulation) corresponds to equilibrium profiles scales $k_x \rho_i \geq 0.2$. This suggests that FLR effects become important for the tertiary mode at pedestal widths comparable to experimental values.

VII. DRIFT WAVE INSTABILITY

The electron drift wave instability can be obtained from Eq. (41) in the case that any or all of the terms proportional to μ , ν , or λ in Ohm's law [Eqs. (3) or (28)] are retained. In the general case of spatially varying profiles of ϕ'_0 , n'_0 , etc., Eq. (28) can be used to eliminate $\tilde{\phi}_e$ from Eq. (41), resulting in a single fourth-order eigenvalue equation for $\tilde{\chi}$. We have solved this equation numerically for pedestal-like equilibrium profiles, and have found results that agree well with the GS2 simulations discussed later in this section. Even in the presence of significant values of the magnetic shear, both analyses predict the existence of well-localized eigenmodes with maximum growth rates that can approach ω_{*e} . In the limit of $k_y L > 1$, where L is the scale of the equilibrium profiles, the growth rates and frequencies obtained from both numerical studies are close to the values predicted by a simple cubic dispersion relation from local theory. Dropping the magnetic shear (justified in Appendix C) we demonstrate this result analytically by showing that fourth-order eigenvalue problem for $k_y L > 1$ may be reduced to a second-order harmonic oscillator equation with a simple Gaussian solution. The resulting dispersion relation, to leading order, is equivalent to that of local theory.

Turning first to the case in which some analytic progress can be made, we consider $k_y L > 1$ where $L^2 \sim |F_0/F'_0|$ and F_0 is any of the equilibrium quantities n'_0 , ϕ'_0 , T'_0 . The x scale of the mode Δ_d will turn out to be smaller than L by a factor of $1/\sqrt{k_y L}$,

$$\Delta_d \sim \sqrt{\frac{L}{k_y}} < L, \quad (81)$$

which allows for several simplifications. First, the left-hand side of Eq. (41) can be written as

$$\partial_x \left[\bar{\gamma} \bar{\gamma}_i \partial_x \left(\frac{\tilde{\phi}_e}{\bar{\gamma}_e} \right) \right] - k_y^2 \bar{\gamma} \bar{\gamma}_i \frac{\tilde{\phi}_e}{\bar{\gamma}_e} \approx \bar{\gamma} \bar{\gamma}_i \nabla^2 \frac{\tilde{\phi}_e}{\bar{\gamma}_e} + \dots \quad (82)$$

or eliminating $\tilde{\phi}_e$ with Eq. (28) and collecting terms

$$B(x) \tilde{J}'' = [A(x) + k_y^2 B(x)] \tilde{J}, \quad \tilde{J} = \nabla_{\perp}^2 \tilde{\chi}, \quad (83)$$

where $\tilde{J}'' = \partial_x^2 \tilde{J}$ and

$$A(x) = \bar{\gamma}_e (\alpha \bar{\gamma} \bar{\gamma}_i + k_{\parallel}^2), \quad (84)$$

$$B(x) = \bar{\gamma} \bar{\gamma}_i (\mu \bar{\gamma} + \nu + \lambda |k_{\parallel}|) + k_{\parallel}^2 \rho_s^2 (\bar{\gamma}_i + \tau \bar{\gamma}_e). \quad (85)$$

In addition, given $\Delta_d < L$, the equilibrium quantities n'_0 , ϕ'_0 , T'_{i0} can be Taylor-expanded about the point where the mode is localized. We assume for simplicity that these quantities all have maxima at the same spatial location $x=0$, and we neglect the magnetic shear, so that $k_{\parallel} = \text{const}$. [All of the equilibrium profiles need not vary spatially, however. For example, we find that a spatial well in either the $\mathbf{E} \times \mathbf{B}$ velocity profile ($\phi''_0 \neq 0$), or the plasma gradients (e.g., $n''_0 \neq 0$), or both yield a well-localized solution with a growth rate close to that of local theory.] We therefore write

$$n'_0(x) \approx n'_0(0) + n'''_0(0)x^2/2 + \dots, \quad (86)$$

$$\phi'_0(x) \approx \phi'_0(0) + \phi'''_0(0)x^2/2 + \dots, \quad (87)$$

$$T'_{i0}(x) \approx T'_{i0}(0) + T'''_{i0}(0)x^2/2 + \dots, \quad (88)$$

$$A(x) \approx A(0) + A''(0)x^2/2 + \dots, \quad (89)$$

$$B(x) \approx B(0) + B''(0)x^2/2 + \dots. \quad (90)$$

Substituting these into Eq. (83), and ordering

$$A(0) \sim k_y^2 B(0), \quad \frac{1}{L^2} \ll \frac{\partial_x^2 \tilde{J}}{\tilde{J}} \sim \frac{1}{\Delta_d^2} \sim \frac{k_y}{L} \ll k_y^2, \quad (91)$$

one finds that the only way that Eq. (83) can be satisfied is if

$$A(0) + k_y^2 B(0) \approx 0 + \dots \quad (92)$$

or using Eqs. (84) and (85) (evaluated at $x=0$),

$$\bar{\gamma} \bar{\gamma}_i = - \frac{k_{\parallel}^2 [\bar{\gamma}_e + k_y^2 \rho_s^2 (\bar{\gamma}_i + \tau \bar{\gamma}_e)]}{\alpha \bar{\gamma}_e + (\mu \bar{\gamma} + \nu + \lambda |k_{\parallel}|) k_y^2}. \quad (93)$$

This result, a cubic polynomial to be solved for γ , is the local dispersion relation mentioned earlier. As a result of Eq. (92), it is necessary to keep the next-order terms in the Taylor

expansion of A and B only on the right-hand side of Eq. (83), yielding

$$\tilde{J}'' = (c_2 + c_1 x^2) \tilde{J}, \quad (94)$$

where

$$c_2 = \frac{A(0) + k_y^2 B(0)}{B(0)}, \quad c_1 = \frac{A''(0) + k_y^2 B''(0)}{2B(0)}. \quad (95)$$

Equation (94) is the harmonic oscillator equation, with the lowest order solution

$$\tilde{J} \propto e^{-\sqrt{c_1} x^2/2}, \quad (96)$$

where c_1 and c_2 must be related by

$$c_2 = -\sqrt{c_1}. \quad (97)$$

The consistency of Eq. (97) with Eq. (92) can be seen by noting that $\sqrt{c_1} \sim k_y/L$ is much smaller than the natural scale of the terms in $c_2 \sim k_y^2$. To leading order Eq. (97) therefore reduces to $c_2 \approx 0$, which is equivalent to Eq. (92). One can also verify that the ordering given in Eq. (91) is consistent with Eq. (94). Estimating $\tilde{J}'' \sim (1/\Delta_d^2) \tilde{J} \sim (k_y/L) \tilde{J}$, $x^2 \sim \Delta_d^2$, $c_1 \sim k_y^2/L^2$, and $c_2 = -\sqrt{c_1} \sim k_y/L$, all the terms in Eq. (94) are found to be of the same order, as one would expect. Finally, consistent with Eq. (81), one sees from Eq. (96) that the x scale of the mode is $\Delta_d \sim c_1^{-1/4} \sim \sqrt{L/k_y}$, as claimed.

The spatial localization of the eigenfunction in Eq. (96) requires that $\text{Re}(\sqrt{c_1}) > 0$. When calculating $\sqrt{c_1}$ from c_1 given in Eq. (95), however, the overall sign of $\sqrt{c_1}$ is not determined. Provided that $\text{Re}(\sqrt{c_1}) \neq 0$, therefore, it is always possible to choose this sign so that $\text{Re}(\sqrt{c_1}) > 0$. The exceptional case of $\text{Re}(\sqrt{c_1}) = 0$, which is obtained when c_1 is real and negative, cannot arise provided that the local dispersion relation [Eq. (92)] predicts instability for the parameters under consideration. To see this, note that c_1 can be determined to leading order by solving the local dispersion relation [Eq. (92)] for γ , and substituting the result into the expression for c_1 given by Eq. (95). Inspection of c_1 then shows that it will always be complex provided that $\text{Re}(\gamma) \neq 0$.

We now turn to a comparison of the analytic results to GS2 simulations and numerical solutions of Eq. (41). The GS2 simulations are based on the simple periodic slab geometry discussed in Sec. IV. Our procedure is to allow the simulations to settle into an equilibrium with $k_y = 0$, and then look at the stability of this state to a spectrum of small finite- k_y perturbations. We first consider the parameters $V_E = 114$, $V_{*en} = -V_{*in}/\tau = -240$, $V_{*iT} = 0$, $\tau = 0.05$, $\beta_e = 0$, $m_e/m_i = 2.7 \times 10^{-4}$, $k_x = 0.05$, and $k_{\parallel} = 7.5$. Plots of $\text{Re}(\gamma)$ and $\omega = -\text{Im}(\gamma)$ as a function of k_y are shown in Fig. 5, where the normalizing factor in physical units is $\gamma_0 \equiv c_{se}/L_n$ (in the nonlocal case, L_n is evaluated at point of steepest gradient). The growth rates in the figure, made at fixed $k_{\parallel} = 7.5$, are about a factor of 2 smaller than the maximal values for the mode at these parameters (not shown), which arise at smaller $k_{\parallel} \sim 2$. The solid lines are the local (cubic) dispersion relation [Eq. (92) or Eq. (93)]. The full numerical solution of Eq. (41) as well as the next-order dispersion relation [Eq. (97)] (not shown) yield similar results. The triangles represent the non-

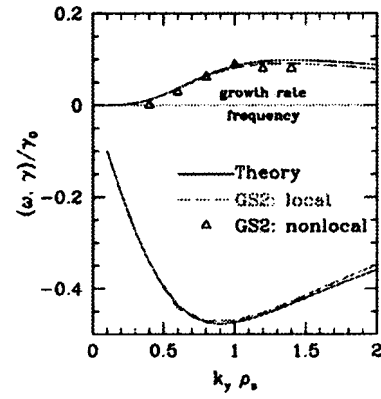


FIG. 5. Drift wave mode γ vs k_y .

local GS2 growth rate, without magnetic shear. The dashed lines indicate the GS2 results in the local limit with no magnetic shear, in which the gradients are spatially constant (equal to the maximum values at the “center” of the pedestal in the nonlocal case). It is evident that the theory correctly predicts the growth rate of the drift wave instability with or without radially varying $\mathbf{E} \times \mathbf{B}$ shear.²⁰ Finally, we have also numerically verified the theoretical results regarding the impact of magnetic shear, i.e., for typical barrier configurations considered elsewhere in this paper, the magnetic shear has no significant effect on the growth rate of the drift wave for $0 < \hat{s} < 3$. This numerically verified insensitivity to \hat{s} is consistent with estimates described in Appendix C [for example, Eq. (C4)].

According to the analytic dispersion relation and consistent with the simulations, the most unstable mode at typical H -mode pedestal parameters has a growth rate that is significantly reduced due to electromagnetic effects (finite β_e) and is driven almost entirely by electron Landau damping. These points are demonstrated in Fig. 6. The left plot shows γ obtained from GS2 for various β_e values, using the same parameters as before, except with $k_{\parallel} = 1.5$. On the right we show growth rates maximized over k_{\parallel} , at fixed $k_y \rho_s = 0.6$. This figure shows that electron Landau damping, while stabilizing at lower β_e values, can be the main driver of instability at larger β_e (e.g., those typical of experiments).

In addition, as one would expect given the radially localized nature of the mode, the instability is only weakly sensitive to the detailed form of the profiles. For example, in

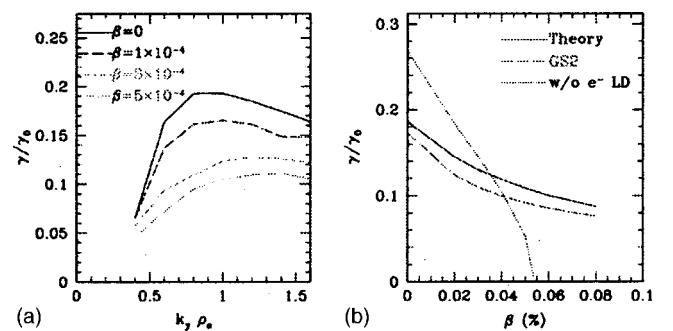


FIG. 6. Drift wave growth rate γ vs (a) k_y , and (b) β_e .

the numerical study of Eq. (41), we have analyzed both the periodic profiles of Eq. (43) as well a hyperbolic-tangent model-like Eq. (59), and find that the difference between the two [for fixed values of $\phi_0'''(0)$, $n_0'''(0)$, $T_0'''(0)$] is negligible.

Lastly, it should be noted that although the presence of magnetic shear appears to eliminate the presence of linearly unstable eigenmodes in the local GS2 simulations (as one would expect), substantial transient growth (e.g., due to convective modes) in this case is still observed. Indeed, for typical H -mode edge parameters, the amplification factor observed in the GS2 simulations of small initial perturbations can be quite large. Further work that also includes nonlinear simulations is in progress to determine the role of such convective modes.

VIII. SUMMARY OF MAIN RESULTS

We have analyzed the linear stability of a slab geometry containing spatially varying $\mathbf{E} \times \mathbf{B}$ and diamagnetic flows in a sheared magnetic field, similar to the profiles found in the edge region of high temperature (H mode) magnetically confined plasmas. Strong parallel flows, though sometimes present in experiments, were not addressed. We have presented the results of gyrokinetic simulations using the GS2 code, as well as analytic calculations based on the Braginskii and gyrofluid models. The analytic calculations are limited to the regime of $k_{\perp}^2 \rho_i^2 \ll 1$. In this regime, the Braginskii and gyrofluid models yield equivalent results, and show good overall agreement with the simulations. Some other assumptions and limitations of the study are outlined in the Introduction.

We find at least three linear modes of potential importance in such systems: the Kelvin–Helmholtz instability, the tertiary mode, and a nonlocal drift wave instability. All three modes are unstable only in presence of nontrivial spatial variations in either the $\mathbf{E} \times \mathbf{B}$ flow and/or the plasma gradients. Our main results in each case are as follows.

A. Kelvin–Helmholtz instability

This instability is driven by the spatial variations in the $\mathbf{E} \times \mathbf{B}$ velocity V_E . In the absence of magnetic shear and ion diamagnetic effects, the most unstable eigenmode has a typical growth rate $\gamma \sim V_E/L$, where L is the scale of spatial variations in V_E , a wave number $k_y \sim 1/L$ in the direction of V_E , a width $\Delta \sim L$ in the direction of variation (e.g., radial direction in a tokamak), and $k_{\parallel} = 0$. It can be stabilized by magnetic shear if the profile widths ($\sim L$) are sufficiently wide [see Eq. (68), for example]. It can also be stabilized by ion diamagnetic effects if the ion diamagnetic velocity V_{*i} is at least comparable in magnitude to V_E and in the opposite direction over the envelope of the mode, such that $V_E(V_E + V_{*i}) < 0$. The assumption of an adiabatic electron response, sometimes made in simulations of small-scale turbulence, completely suppresses this instability. This may account for why the KH mode has thus far not been greatly emphasized by the microscale simulation community. According to our rough estimates, it is near marginal stability under typical H -mode edge conditions, and thus a more detailed study based on a realistic magnetic geometry is necessary to assess

its true role. The possible role of KH modes in ITBs depends critically upon the details of the velocity profile, which are not well known. It is likely, however, that KH instabilities play some role in ITB phenomenology.

B. Tertiary mode

This is an adiabatic electron, electrostatic mode arising at higher k_{\parallel} that is driven by the ion temperature gradient. It also has a complex dependence on the density gradient. Assuming the $\mathbf{E} \times \mathbf{B}$ velocity V_E and the ion diamagnetic velocity V_{*i} are comparable in magnitude, it has a typical width $\Delta \sim \sqrt{\rho_s L}$ in the direction of profile variation and a growth rate that is smaller than that of the Kelvin–Helmholtz mode by a factor of $\sim \sqrt{\rho_s/L}$ (only a modest reduction for typical H -mode pedestals). According to the GS2 simulations, the mode is stabilized by finite Larmor radius effects for pedestal scale lengths that approach experimentally observed values. Put another way, for narrow pedestals, the tertiary instability growth rate *increases* as the pedestal widens. Like the Kelvin–Helmholtz mode, further nonlinear simulations are needed to determine its true importance in the tokamak edge.

C. Nonlocal drift wave mode

This mode is driven by either electron inertia, electron-ion collisionality, or electron Landau damping and, like the previous case, also has finite k_{\parallel} . It is robustly unstable in the presence of magnetic and $\mathbf{E} \times \mathbf{B}$ shear at typical H -mode edge discharge levels. The eigenmode is spatially localized by extrema in either the $\mathbf{E} \times \mathbf{B}$ velocity or the density gradient, and at higher wave numbers at which a local treatment becomes valid (e.g., $k_y L > 1$) has a growth rate given by Eq. (93). The most unstable mode has a frequency that is comparable to ω_{*e} in a frame that rotates with the local $\mathbf{E} \times \mathbf{B}$ velocity. Under typical H -mode conditions, its growth rate is significantly reduced by electromagnetic effects, which become important at finite plasma β , and electron Landau damping plays an essential destabilizing role. An accurate description of this mode therefore requires a model that includes electron Landau damping effects, as well as electromagnetic effects and nonlocal profile variations. This mode seems to be a good candidate for driving particle and heat transport in the H -mode edge, in which curvature-driven modes are known to become weak due to diamagnetic stabilization, or in the edge of linear devices.

ACKNOWLEDGMENTS

This work was supported by the Center for Multiscale Plasma Dynamics, the U.S. Department of Energy Grant No. DE-FC02-04ER54784 and NSF Grant No. 0238694.

APPENDIX A: VALIDITY OF THE ADIABATIC APPROXIMATION

To see when the adiabatic approximation is valid, consider using Eq. (27) to estimate $\tilde{\chi}$ in the adiabatic limit:

$$\tilde{\chi} \sim \frac{i\bar{\gamma}_e}{k_{\parallel}k_{\perp}^2\rho_s^2}\tilde{\phi}. \quad (\text{A1})$$

The magnitude of the nonadiabatic response $\tilde{\phi}_e$ can now be estimated from Ohm's law [Eq. (28)] as

$$\tilde{\phi}_e \sim \frac{\alpha\bar{\gamma}_e^2 + \bar{\gamma}_e(\mu\bar{\gamma} + \nu + \lambda|k_{\parallel}|)k_{\perp}^2}{k_{\parallel}^2k_{\perp}^2\rho_s^2}\tilde{\phi}. \quad (\text{A2})$$

Thus, $\tilde{\phi}_e \ll \tilde{\phi}$ will be valid when

$$\alpha\bar{\gamma}_e^2 + \bar{\gamma}_e(\mu\bar{\gamma} + \nu + \lambda|k_{\parallel}|)k_{\perp}^2 \ll k_{\parallel}^2k_{\perp}^2\rho_s^2 \quad (\text{A3})$$

or in physical (non-normalized) units,

$$\bar{\gamma}_e^2 + \bar{\gamma}_e\left(\bar{\gamma} + \nu_{ei} + \sqrt{\frac{\pi}{2}}v_{\text{the}}|k_{\parallel}|\right)k_{\perp}^2d_e^2 \ll k_{\parallel}^2c_A^2k_{\perp}^2\rho_{se}^2. \quad (\text{A4})$$

APPENDIX B: BRAGINSKII VERSUS GYROFLUID MODELS

In this appendix, we show how Eq. (41) can be recovered in the gyrofluid formalism. In the first section, we rewrite Eq. (41) in terms of the guiding center potential ψ . In the second section, we explain how this same result can be obtained from the gyrofluid model. In the third section, we give a more general proof of the equivalence of the two models to the order of $k_{\perp}^2\rho_i^2$ that we are working.

1. Equation (41) in gyrofluid notation

To make contact with the gyrofluid model, we first introduce some new notations,

$$\tilde{\Phi} = \frac{\rho_s^2\nabla_{\parallel}J}{\bar{\gamma}_e}, \quad (\text{B1})$$

$$\tilde{\Psi} = \Gamma_0^{1/2}\tilde{\Phi}\left(1 + \frac{1}{2}\tau\rho_s^2\nabla_{\perp}^2 + \dots\right)\tilde{\Phi}, \quad (\text{B2})$$

$$\psi = \Gamma_0^{1/2}\phi = \left(1 + \frac{1}{2}\tau\rho_s^2\nabla_{\perp}^2 + \dots\right)\phi, \quad (\text{B3})$$

$$\bar{\gamma}_{e,\psi} = \Gamma_0^{1/2}\bar{\gamma}_e \quad (\text{B4})$$

$$= \gamma + ik_y(\psi'_0 - \Gamma_0^{1/2}n'_0) \quad (\text{B5})$$

$$= \gamma + ik_y(\psi'_0 - n'_0) - \frac{1}{2}ik_y\tau\rho_s^2n''_0 + \dots \quad (\text{B6})$$

Here, ψ is the guiding center potential, and $\Gamma_0 = I_0(b)e^{-b}$ where $b = \tau\rho_s^2\nabla_{\perp}^2$ and $I_0(b) = J_0(ib)$ is the modified Bessel function. Recall from Eq. (27) that in the adiabatic limit $\tilde{\Phi} \rightarrow \tilde{\phi}$, so that $\tilde{\Psi} \rightarrow \tilde{\psi}$. Operating on Eq. (41) with $\Gamma_0^{1/2}$, ignoring the $k_{\perp}^2\rho_i^2$ corrections to the left-hand side, and noting that

$$\Gamma_0^{1/2}\left[\nabla_{\parallel}J - \partial_x\left(\tau\bar{\gamma}_e\frac{\rho_s^2\nabla_{\parallel}J}{\bar{\gamma}_e}\right)\right] = \left(\frac{\bar{\gamma}_{e,\psi}}{\rho_s^2} - \tau\bar{\gamma}_e''\right)\tilde{\Psi} + \dots, \quad (\text{B7})$$

Eq. (41) can be written as

$$\partial_x\left[\bar{\gamma}\bar{\gamma}_i\partial_x\left(\frac{\tilde{\phi}_e}{\bar{\gamma}_e}\right)\right] - k_y^2\bar{\gamma}\bar{\gamma}_i\frac{\tilde{\phi}_e}{\bar{\gamma}_e} = F_{\parallel}, \quad (\text{B8})$$

$$F_{\parallel} = -\partial_x\left[\bar{\gamma}(\bar{\gamma}_i + \tau\bar{\gamma}_e)\partial_x\left(\frac{\tilde{\Psi}}{\bar{\gamma}}\right)\right] + \left[\frac{\bar{\gamma}_{e,\psi}}{\rho_s^2} - \tau\bar{\gamma}_e'' + k_y^2(\bar{\gamma}_i + \tau\bar{\gamma}_e)\right]\tilde{\Psi}. \quad (\text{B9})$$

Note that all the $\bar{\gamma}$'s here except the $\bar{\gamma}_{e,\psi}$ term depend on ϕ_0 rather than on $\psi_0 (= \phi_0 + \tau\rho_s^2\phi_0''/2 + \dots)$. To the order that we are working here, however, the difference between these is negligible. The only exception where this would not be the case is the $\bar{\gamma}_{e,\psi}$ term, which is formally a factor of $1/(k_{\perp}\rho_s)^2$ larger than the other terms.

Finally, in the adiabatic limit ($\tilde{\phi}_e \rightarrow 0, \Psi \rightarrow \psi$) and considering $n'_0 = 0$, note this is the same as Eq. (6) of Ref. 2, in which the tertiary mode was first discussed.

2. Gyrofluid ion model

Dropping terms of order $(k_{\perp}\rho_i)^4$ compared to unity, the gyrofluid model we consider is given by^{21,22}

$$d_t n_g + \frac{1}{2}[\tau\rho_s^2\nabla_{\perp}^2\psi, T_{\perp}] = 0, \quad (\text{B10})$$

$$d_t T_{\perp} = 0, \quad (\text{B11})$$

$$n_g = n - \rho_s^2\nabla_{\perp}^2[\psi + \tau(n + T_{\perp})/2], \quad (\text{B12})$$

$$d_t = \partial_t + [\psi, \cdot], \quad [a, b] = \hat{z} \cdot \nabla_{\perp} a \times \nabla_{\perp} b. \quad (\text{B13})$$

To make contact with Eq. (B8) we need to express everything in terms of $\tilde{\Psi}$ and $\tilde{\phi}_e$. First consider the electron density n . Writing $n = n_0 + \tilde{n}$ and using Eqs. (24) and (B2) one obtains

$$\begin{aligned} \tilde{n} &= ik_y n'_0 \frac{\tilde{\phi}_e}{\bar{\gamma}_e} + \Gamma_0^{-1/2}\tilde{\Psi} \\ &= ik_y n'_0 \frac{\tilde{\phi}_e}{\bar{\gamma}_e} + \left(1 - \frac{1}{2}\tau\rho_s^2\nabla_{\perp}^2 + \dots\right)\tilde{\Psi}. \end{aligned} \quad (\text{B14})$$

In this section, as in Eq. (B8) we will retain the non-adiabatic terms only to leading order in $k_{\perp}^2\rho_i^2$ (but treating $\phi \sim \tau p_i$), so we do not need to worry about the difference between ϕ_0 and ψ_0 in $\bar{\gamma}_e$ here. Next, writing $\psi = \psi_0 + \tilde{\psi}$, and using the definitions of ψ and $\phi_e (= \phi - n)$ and Eq. (B14), one finds

$$\tilde{\psi} = \Gamma_0^{1/2}\tilde{\phi} = \Gamma_0^{1/2}(\tilde{\phi}_e + \tilde{n}) = \tilde{\Psi} + \Gamma_0^{1/2}\left(\bar{\gamma}\frac{\tilde{\phi}_e}{\bar{\gamma}_e}\right). \quad (\text{B15})$$

Likewise, writing $T_{\perp} = T_{\perp 0} + \tilde{T}_{\perp}$ one obtains from Eq. (B11),

$$\tilde{T}_{\perp} = ik_y T'_{\perp 0} \frac{\tilde{\psi}}{\bar{\gamma}} = ik_y T'_{\perp 0} \left(\frac{\tilde{\Psi}}{\bar{\gamma}} + \frac{\tilde{\phi}_e}{\bar{\gamma}_e} + \dots\right). \quad (\text{B16})$$

Here, again, we only need T_{\perp} to leading order in $k_{\perp}\rho_i$. Note that this also allows us to ignore the difference between the guiding center T_{\perp} and the usual fluid T_{\perp} . Finally, writing $n_g = n_{g0} + \tilde{n}_g$, and defining $p_{i0} = n_0 + T_{\perp 0}$, one can substitute Eqs. (B14), (B15), and (B16) into Eq. (B12) to obtain

$$n_{g0} = n_0 - \rho_s^2 [\psi''_0 + \tau p'_{i0}/2], \quad (\text{B17})$$

$$\begin{aligned} \tilde{n}_g = & \tilde{\Psi} + ik_y n'_0 \frac{\tilde{\phi}_e}{\tilde{\gamma}_e} - \rho_s^2 \nabla_{\perp}^2 \left\{ (\bar{\gamma} + ik_y \tau p'_{i0}/2) \frac{\tilde{\phi}_e}{\tilde{\gamma}_e} \right\} \\ & - \rho_s^2 \nabla_{\perp}^2 \left\{ [(1 + \tau) \bar{\gamma} + ik_y \tau T'_{\perp 0}/2] \frac{\tilde{\Psi}}{\tilde{\gamma}} \right\} + \dots \end{aligned} \quad (\text{B18})$$

To obtain Eq. (B8), substitute these results for n_g , ψ , and T_{\perp} into Eq. (B10) and collect terms.

3. General proof of equivalence

Given Eq. (B2) which relates ψ and ϕ , Eqs. (B10)–(B13) may be written as^{21,22}

$$d_t n_g + \frac{1}{2} [\rho_s^2 \nabla_{\perp}^2 \phi, \tau p_{g\perp}] = 0, \quad p_{g\perp} = n_g + T_{g\perp}, \quad (\text{B19})$$

$$n = n_g + \rho_s^2 \nabla_{\perp}^2 \left(\phi + \frac{1}{2} \tau p_{g\perp} \right) + \dots, \quad (\text{B20})$$

$$d_t = \partial_t + [\phi, \cdot], \quad [a, b] = \hat{z} \cdot \nabla_{\perp} a \times \nabla_{\perp} b, \quad (\text{B21})$$

where $p_{g\perp}$ is the guiding center ion (perpendicular) pressure. Operating on Eq. (B20) with d_t and using Eq. (B19) gives

$$d_t n = d_t [\rho_s^2 \nabla_{\perp}^2 \left(\phi + \frac{1}{2} \tau p_{g\perp} \right)] - \frac{1}{2} [\rho_s^2 \nabla_{\perp}^2 \phi, \tau p_{g\perp}]. \quad (\text{B22})$$

One can now use the identity

$$d_t \nabla_{\perp}^2 f = \nabla_{\perp}^2 d_t f - 2[\nabla_{\perp} \phi; \nabla_{\perp} f] - [\nabla_{\perp}^2 \phi, f], \quad (\text{B23})$$

where $[a; b] = [a_x, b_x] + [a_y, b_y]$ to write Eq. (B22) as

$$d_t n = \rho_s^2 \nabla_{\perp} \cdot d_t \nabla_{\perp} \left(\phi + \tau p_{g\perp} \right) - \frac{1}{2} \rho_s^2 \nabla_{\perp}^2 d_t \tau p_{g\perp}. \quad (\text{B24})$$

To obtain agreement with the Braginskii model, it is necessary to retain the $\tau p_{g\perp}$ terms (that is, the ion diamagnetic terms) only to leading order in $k_{\perp}^2 \rho_i^2$. (No assumption will be made here regarding the smallness of $k_{\perp}^2 \rho_s^2$, however.) Noting that $p_{g\perp}$ obeys the equation^{21,22}

$$d_t p_{g\perp} + [\rho_i^2 \nabla_{\perp}^2 \phi, p_{g\perp} + T_{g\perp}] = 0, \quad (\text{B25})$$

where $\rho_i^2 = \tau \rho_s^2$, and that $p_{g\perp}$ is related to the usual fluid p_{\perp} by^{21,22}

$$\tau p_{\perp} = \tau p_{g\perp} + 3\rho_i^2 \nabla_{\perp}^2 \tau p_{g\perp} + \frac{3}{2} \rho_i^2 \nabla_{\perp}^2 \phi + \dots, \quad (\text{B26})$$

one sees that the last term on the right side of Eq. (B24) can be neglected to the order we are working, as can the difference between $p_{g\perp}$ and p_{\perp} in the first term. As a result, given Eq. (1), Eq. (B24) reduces Eq. (31).

APPENDIX C: IMPACT OF MAGNETIC SHEAR ON DRIFT WAVE INSTABILITY

In the case in which equilibrium variation and magnetic shear are both included, it is possible to estimate the point at which magnetic shear effects become significant within the envelope of the drift wave instability, $x \lesssim \Delta_d$. Balancing the two terms in the k_{\parallel} model of Eq. (22) for $x \sim \Delta_d \sim \sqrt{L/k_y}$ gives

$$L_s \sim \sqrt{k_y L} / k_{z,\text{phys}}. \quad (\text{C1})$$

A reasonably accurate description of the fastest growing mode for the parameters discussed in the text may be obtained by writing Eq. (93) as a cubic in $\tilde{\gamma}_e$, and then neglecting the highest order term ($\propto \tilde{\gamma}_e^3$). An analysis of the resulting quadratic then yields the estimate for k_z of the fastest growing mode (at fixed k_y , assuming $k_y^2 \rho_{se}^2 \ll 1$, and neglecting ν_{ei}),

$$k_z^2 \sim (\alpha + \mu k_y^2) k_y^2 n'_0 (n'_0 + \tau p'_{i0}) \quad (\text{C2})$$

or in physical units (assuming $L_n \sim L_{pi} \sim L$)

$$k_{z,\text{phys}} \sim \sqrt{\frac{\beta k_y \rho_{se}}{2L}} (1 + k_y^2 a_e^2)^{1/2} \sim \sqrt{\frac{\beta k_y \rho_{se}}{2L}}. \quad (\text{C3})$$

Substituting this into Eq. (C1) and assuming $L_s = qR/\hat{s}$ yield the threshold condition for magnetic shear to become important,

$$\hat{s} \sim q \frac{R \rho_{se}}{L^2} \sqrt{\frac{\beta}{2}} \sqrt{k_y L} \sim q \frac{R \rho_{se}}{L^2} \sqrt{\beta}. \quad (\text{C4})$$

Taking $L \sim 5\rho_{se}$ and evaluating the right-hand side for the reference edge parameters discussed in the text yield $\hat{s} \sim 7$ (DIII-D or C-MOD), which implies that magnetic shear is unlikely to play a significant role for this mode.

¹W. Dorland, F. Jenko, M. Kotschenreuther, and B. N. Rogers, Phys. Rev. Lett. **85**, 5579 (2000).

²B. N. Rogers, W. Dorland, and M. Kotschenreuther, Phys. Rev. Lett. **85**, 5336 (2000).

³J. Drake, A. Zeiler, and D. Biskamp, Phys. Rev. Lett. **75**, 4222 (1995).

⁴A. Zeiler, D. Biskamp, J. F. Drake, and P. N. Guzdar, Phys. Plasmas **3**, 2951 (1996).

⁵B. D. Scott, Plasma Phys. Controlled Fusion **39**, 1635 (1997).

⁶B. N. Rogers, J. Drake, and A. Zeiler, Phys. Rev. Lett. **81**, 4396 (1998).

⁷T. M. Antonsen, Jr., Phys. Rev. Lett. **41**, 33 (1978).

⁸B. Coppi, Phys. Lett. **14**, 172 (1965).

⁹N. Krall and M. Rosenbluth, Phys. Fluids **8**, 1488 (1965).

¹⁰S. Moiseev and R. Sagdeev, Sov. Phys. Tech. Phys. **9**, 196 (1964).

¹¹J. B. Taylor, in *Plasma Physics and Controlled Nuclear Fusion Research*, Proceedings of the Sixth International Conference, Berchtesgaden, 1976 (IAEA, Vienna, 1977), Vol. 2, p. 323.

¹²L. Chen *et al.*, Nucl. Fusion **19**, 373 (1979).

¹³S. C. Cowley, R. M. Kulsrud, and R. Sudan, Phys. Fluids B **3**, 2767 (1991).

¹⁴D. Pearlstein and H. Berk, Phys. Rev. Lett. **23**, 220 (1969).

¹⁵M. Beer, S. C. Cowley, and G. W. Hammett, Phys. Plasmas **2**, 2687 (1995).

¹⁶G. Hammett and F. Perkins, Phys. Rev. Lett. **64**, 3019 (1990).

¹⁷A. Zeiler, J. F. Drake, and B. Rogers, Phys. Plasmas **4**, 2134 (1997).

¹⁸R. D. Deranian, R. J. Groebner, and D. T. Pham, Phys. Plasmas **7**, 1235 (2000).

¹⁹D. A. Mossessian *et al.*, Plasma Phys. Controlled Fusion **44**, 423 (2002).

²⁰It is more difficult to extract the real frequency from the radially nonlocal simulations. Given the theoretical results and the good match with the growth rate, which is easy to diagnose, we have chosen not to track down this detail.

²¹W. Dorland and G. Hammett, Phys. Fluids B **5**, 812 (1993).

²²P. B. Snyder, Ph.D. thesis, Princeton University, 1999.